Hindawi Publishing Corporation
Journal of Nanomaterials
Volume 2013, Article ID 127345, 9 pages
http://dx.doi.org/10.1155/2013/127345

Research Article

Pd-Doped SnO_2-Based Sensor Detecting Characteristic Fault Hydrocarbon Gases in Transformer Oil

Weigen Chen,[1] Qu Zhou,[1] Tuoyu Gao,[1] Xiaoping Su,[2] and Fu Wan[1]

[1] *State Key Laboratory of Power Transmission Equipment & System Security and New Technology, Chongqing University, Chongqing 400030, China*
[2] *Electric Operations and Control Centers, Chengdu Power Supply Company, Chengdu 610017, China*

Correspondence should be addressed to Qu Zhou; zhouqupsd@yahoo.cn

Received 7 December 2012; Revised 11 January 2013; Accepted 14 January 2013

Academic Editor: Ming-Guo Ma

Methane (CH_4), ethane (C_2H_6), ethylene (C_2H_4), and acetylene (C_2C_2) are important fault characteristic hydrocarbon gases dissolved in power transformer oil. Online monitoring these gaseous components and their generation rates can present the operational state of power transformer timely and effectively. Gas sensing technology is the most sticky and tricky point in online monitoring system. In this paper, pure and Pd-doped SnO_2 nanoparticles were synthesized by hydrothermal method and characterized by X-ray powder diffraction, field-emission scanning electron microscopy, and energy dispersive X-ray spectroscopy, respectively. The gas sensors were fabricated by side-heated preparation, and their gas sensing properties against CH_4, C_2H_6, C_2H_4, and C_2H_2 were measured. Pd doping increases the electric conductance of the prepared SnO_2 sensors and improves their gas sensing performances to hydrocarbon gases. In addition based on the frontier molecular orbital theory, the highest occupied molecular orbital energy and the lowest unoccupied molecular orbital energy were calculated. Calculation results demonstrate that C_2H_4 has the highest occupied molecular orbital energy among CH_4, C_2H_6, C_2H_4, and C_2H_2, which promotes charge transfer in gas sensing process, and SnO_2 surfaces capture a relatively larger amount of electric charge from adsorbed C_2H_4.

1. Introduction

With the development of ultra-high voltage and extra-high voltage electricity transmission and transformation project [1, 2], the quantity and capacity of power transformers with various voltage levels sharply increase. Power transformers are essential electrical apparatus, and their operating conditions directly affect the safety and reliability of the power system [3–5]. Faults happened in power transformers bring huge economic losses to our national economy [6]. Now, most of the large power transformers are in oil-paper insulation structures. When internal insulation faults occur in a transformer, the transformer generates some low molecular hydrocarbon gases [7–9], such as methane (CH_4), ethane (C_2H_6), ethylene (C_2H_4), and acetylene (C_2H_2), and most of these gaseous components are dissolved in transformer oil. Online monitoring the component contents of these dissolved hydrocarbon gases and their generation rates is one of the most effective and convenient methods for diagnosing transformer incipient faults. This method can distinguish different types of faults which happened in power transformer, such as overheating, partial discharge, spark discharge, and arcing discharge [10–13].

Gas sensing technology is the core of online monitoring. At present, semiconductor gas sensors [14, 15], palladium gate field effect transistors [16], catalytic combustion sensors [17, 18], fuel cell sensors [19], and optical sensors [20, 21] are mainly methods utilized to detect characteristic fault gases. Given remarkable advantages of simple fabrication process, low maintenance cost, rapid response and recovery time, long service life [22], metal oxide semiconductor materials like SnO_2 [22], ZnO [23], TiO_2 [24], and In_2O_3 [25] have been receiving scientific and technological importance for many years [26, 27] and widely used to detect flammable, explosive, and poisonous gases. However, when used to detect hydrocarbon gases traditional SnO_2-based gas sensor

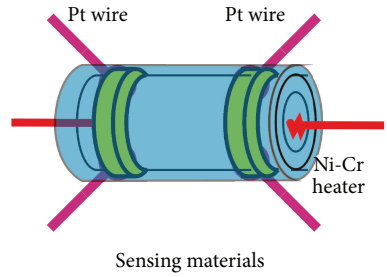

Figure 1: The structure of a side-heated gas sensor.

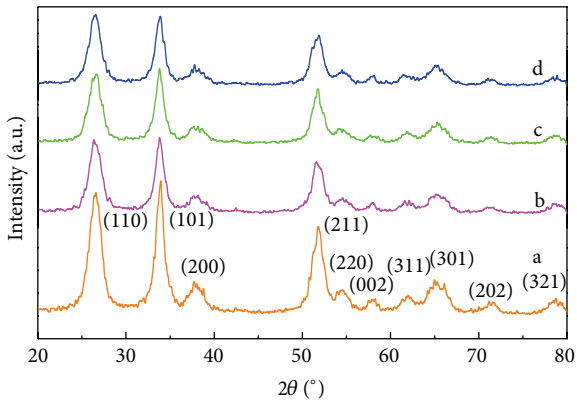

Figure 2: XRD patterns of (a) pure, (b) 1 wt%, (c) 3 wt%, and (d) 5 wt% Pd-doped SnO_2 nanoparticles.

presents some limitations such as low gas response and high operating temperature [28]. Many relevant studies have been conducted to enhance the sensing performances of SnO_2 [29–31]. Doping noble metal is an effective method to improve the gas sensing properties of conventional thick or thin film gas sensor [32, 33]. However, due to the same composition and similar structure for the four hydrocarbons, the gas sensing mechanism is still unclear and lack detail understandings.

In this work, SnO_2 samples doped with metallic ions Pd^{2+} (1, 3, and 5 wt%) were prepared using a simple hydrothermal synthesis route. The crystalline structures, chemical compositions, and surface morphologies of the prepared samples were performed by X-ray powder diffraction (XRD), field-emission scanning electron microscopy (FESEM), and energy dispersive X-ray spectroscopy (EDS), respectively; as well as their gas sensing properties to CH_4, C_2H_6, C_2H_4, and C_2H_2 were measured. Furthermore, the highest occupied molecular orbital (HOMO) and the lowest unoccupied molecular orbital (LOMO) of hydrocarbon gases and the density of states (DOS) of SnO_2 (110) surface were calculated.

2. Experimental

2.1. Preparation and Characterization of Materials. Pure and Pd-doped SnO_2 powders were prepared by hydrothermal method using$SnCl_4{\cdot}5H_2O$, $Na_2SO_4{\cdot}5H_2O$, $PdCl_2{\cdot}2H_2O$, NaOH, absolute ethanol, and distilled water as precursors. All chemical reagents were of analytical grade and purchased from Beijing Chemicals Co. Ltd. In this study, 0.903 g of NaOH, 1.262 g of $SnCl_4{\cdot}5H_2O$, 0.3 g of $Na_2SO_4{\cdot}5H_2O$, 30 mL of absolute ethanol, and 30 mL of distilled water were mixed together. Then, the compound metal salt $PdCl_2{\cdot}2H_2O$ was added drop by drop to the mixed solution with intense magnetic stirring. The mass ratio of the total metallic ions added was estimated in a molar ratio of 1, 3, and 5 wt%, respectively. The reaction mixtures were magnetically stirred for about 30 min and then transferred into a 100 mL Teflon autoclave. The vessel was sealed and heated at 180°C for 24 h in an electric furnace. The prepared products were centrifuged and then washed several times with distilled water and absolute ethanol until Cl^- could not be detected by 0.1 mol/L $AgNO_3$ aqueous solutions. Finally, the products were further air-dried for further characterization.

The crystalline structures of the products were investigated using X-ray powder diffraction. The surface morphologies of both pure and Pd-doped SnO_2 samples were characterized by field-emission scanning electron microscopy. An energy dispersive X-ray spectroscopy analysis was utilized to confirm the chemical compositions of the prepared samples.

2.2. Fabrication and Measurement of Sensors. To fabricate the sensors, the synthesized samples were mixed with absolute ethanol and distilled water at a weight ratio of 80 : 10 : 10 to form a paste. The paste was then screen-printed on an Al_2O_3 ceramic tube, in which a pair of gold electrodes was previously printed. And an Ni-Cr heating wire was inserted into the tube to form a side-heated gas sensor. Figure 1 shows the structure of a side-heated gas sensor.

Its gas sensing properties were measured by a chemical gas sensor-8 (CGS-8) intelligent gas sensing analysis system (Beijing Elite Tech Co., Ltd., China). The sensors were preheated at different operating temperatures for about 30 min. When electric resistances of all the sensors were stable, a targeted gas was injected into the test chamber (20 L in volume) by a microinjector through a rubber plug. The targeted gas was mixed with air by using two fans in the analysis system. After the sensor resistance values reached a new constant value, the test chamber was opened to recover the sensors. All measurements were performed in a laboratory fume hood. Sensor electric resistance and gas response values were automatically acquired by the analysis system. The whole

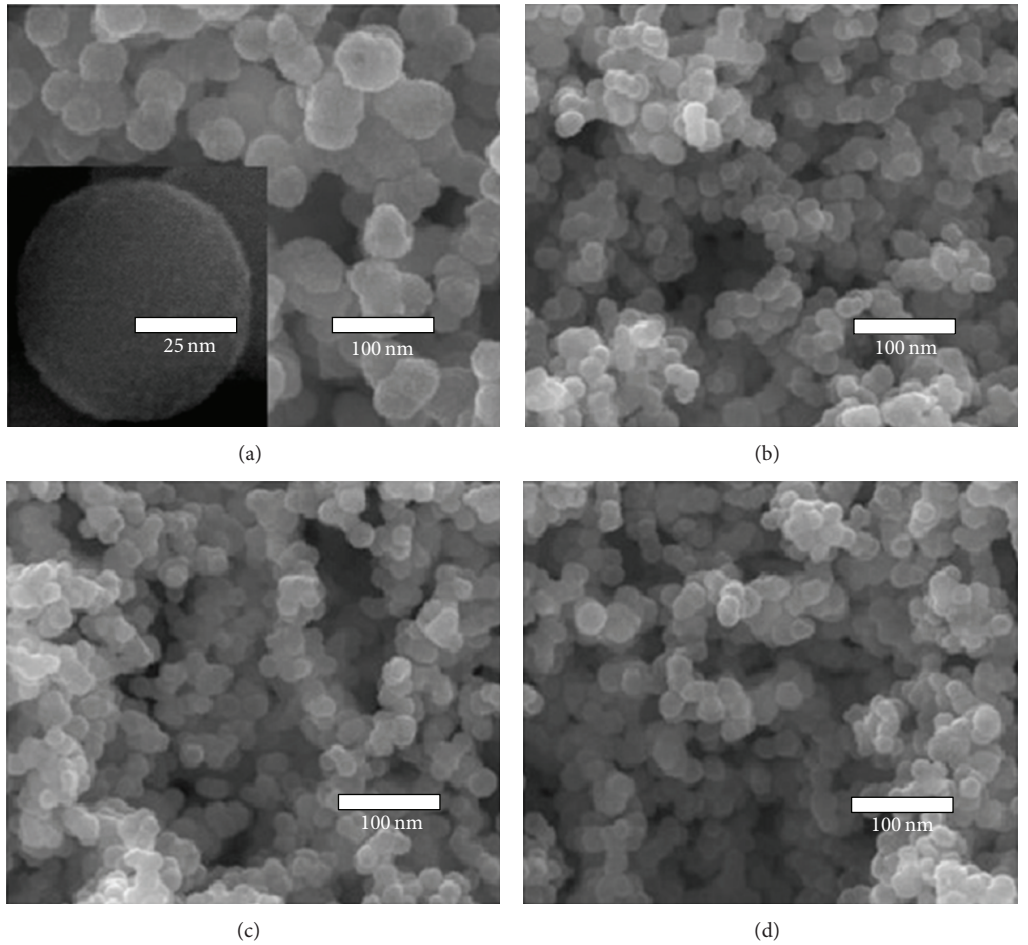

Figure 3: FESEM images of (a) pure, (b) 1 wt%, (c) 3 wt%, and (d) 5 wt% Pd-doped SnO_2 nanoparticles.

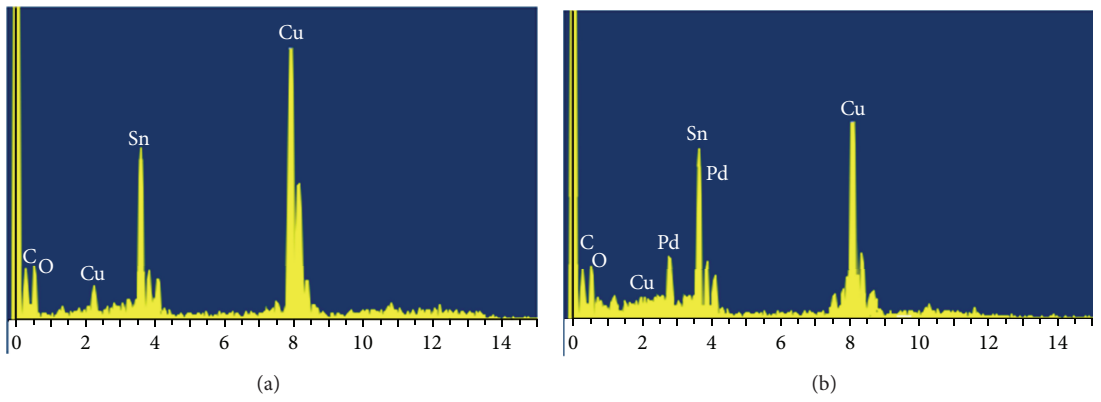

Figure 4: EDS spectra of (a) pure and (b) 3 wt% Pd-doped SnO_2 nanoparticles.

experiment process was performed in a clean room with constant humidity and temperature, which were monitored by the analysis system.

The relative variation of the gas response was defined as $S = (R_0 - R)/R_0$, where R_0 and R represent the resistance of the sensor in air and in targeted gas, respectively. Response time and recovery time were defined as the time taken by the sensor to reach 90% of the total resistance change when gas in and 10% when gas out, respectively. All measurements were repeated several times in order to ensure the reproducibility of the gas sensing response.

2.3. Theoretical Calculation Method. The orbital energy was calculated with the DMol^3 module, which is based on the

linear combination of the atomic orbits. The exchange-correlation function between electrons is described by the revised Perdew-Burke-Ernzerh form of the generalized gradient approximation [34–36]. The orbital cutoff quality was set as 4.3 Å, and the maximum root-mean-square convergent tolerance is 1.0×10^{-6} eV/atom. The basis set was approximated with a double numerical orbit base group and an orbit polarization function to handle the p orbit polarization of hydrogen atom.

3. Results and Discussions

3.1. Structural Characterization. X-ray powder diffraction patterns of the synthesized pure and Pd-doped (1, 3, and 5 wt%) SnO_2 samples were shown in Figure 2. It is obvious that the prominent peaks of (110), (101), (211), and other smaller peaks are corresponding to the standard data file of rutile SnO_2 (JCPDS 41–1445). As the amount of metallic ions doped in SnO_2 is small, no other metal-oxide diffraction features were observed in the patterns. With the amount of metallic ions doped in SnO_2 increasing, the relative intensity of the diffraction peaks decreases, and the full width at half maximum increases. Based on the Scherrer equation $D = 0.89\gamma/(\beta \cos\theta)$, where γ presents the X-ray wavelength, β means the half peak width, and θ is the Bragg angle, the calculated average particle size of pure SnO_2 samples is about 50 nm, and it is about 35–40 nm for Pd-doped SnO_2 samples.

Field-emission scanning electron microscopy was used for characteristic surface morphologies of the prepared samples. One can clearly see in Figure 3 that the crystal particles of prepared samples are uniform in size and have a nearly spherical shape. As shown in Figure 3(a), the average size of pure SnO_2 nanospheres is about 50 nm, and the image inset in Figure 3(a) presents a high-resolution image of a single nanosphere. As seen in Figures 3(b)–3(d), the diameters of the sphere-like Pd-doped SnO_2 samples are ranging from 25 to 30 nm. From these images, it is clearly seen that doping a moderate amount of noble metallic ions Pd^{2+} affects the shapes of SnO_2 slightly but inhibits the crystalline growth of the samples evidently.

In order to further check whether metallic ions Pd^{2+} were successfully doped into the SnO_2 particles, energy dispersive X-ray spectroscopy was used to confirm the elemental chemical compositions of the prepared samples. Figure 4 shows the EDS spectra of pure and 3 wt% Pd-doped SnO_2 nanoparticles. As shown in Figure 4(a), the EDS spectra reveal the elemental compositions of Sn, O, C, and Cu, and no other peaks have been found. Nevertheless, the presence of Pd element is confirmed in the EDS date of Figure 4(b), and the atomic percentage of Pd in the samples is calculated to be about 3 wt%.

3.2. Gas Sensing Properties. Figure 5 shows the electric resistance properties of the prepared SnO_2-based sensors at different temperatures in pure air. As seen in Figure 5, the resistance values of all the sensors decrease when the working temperature increases from 200 to 500°C, which is the intrinsic characteristic of a semiconductor gas sensor. It is also observed that the resistance of the SnO_2 sensor decreases somewhat after Pd^{2+} ions doping. When worked at a same temperature, the electric resistance value decreases in the order of pure 1, 3, and 5 wt% Pd-doped SnO_2 sensors, which means doping a moderate amount of noble metal can improve the electric conductivity of our prepared sensor, and 5 wt% is the optimum doping content among our samples.

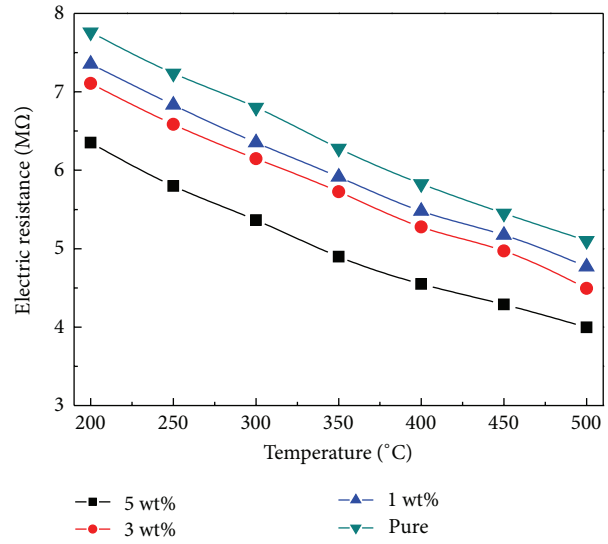

Figure 5: The electric resistance properties of the prepared sensors to different temperatures in air (room temperature at 25°C and relative humidity as 60%).

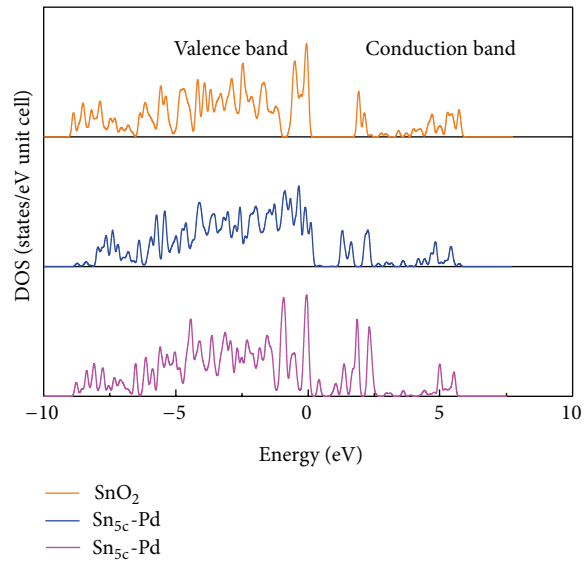

Figure 6: DOS of SnO_2 (110) surface before and after Pd^{2+}-doping.

It is well known that gas sensing performances of metal oxide semiconductor gas sensor are attributed to the changes of electric conductance and particularly dominantly controlled by band structure, conduction band, and valence band near the Fermi level.

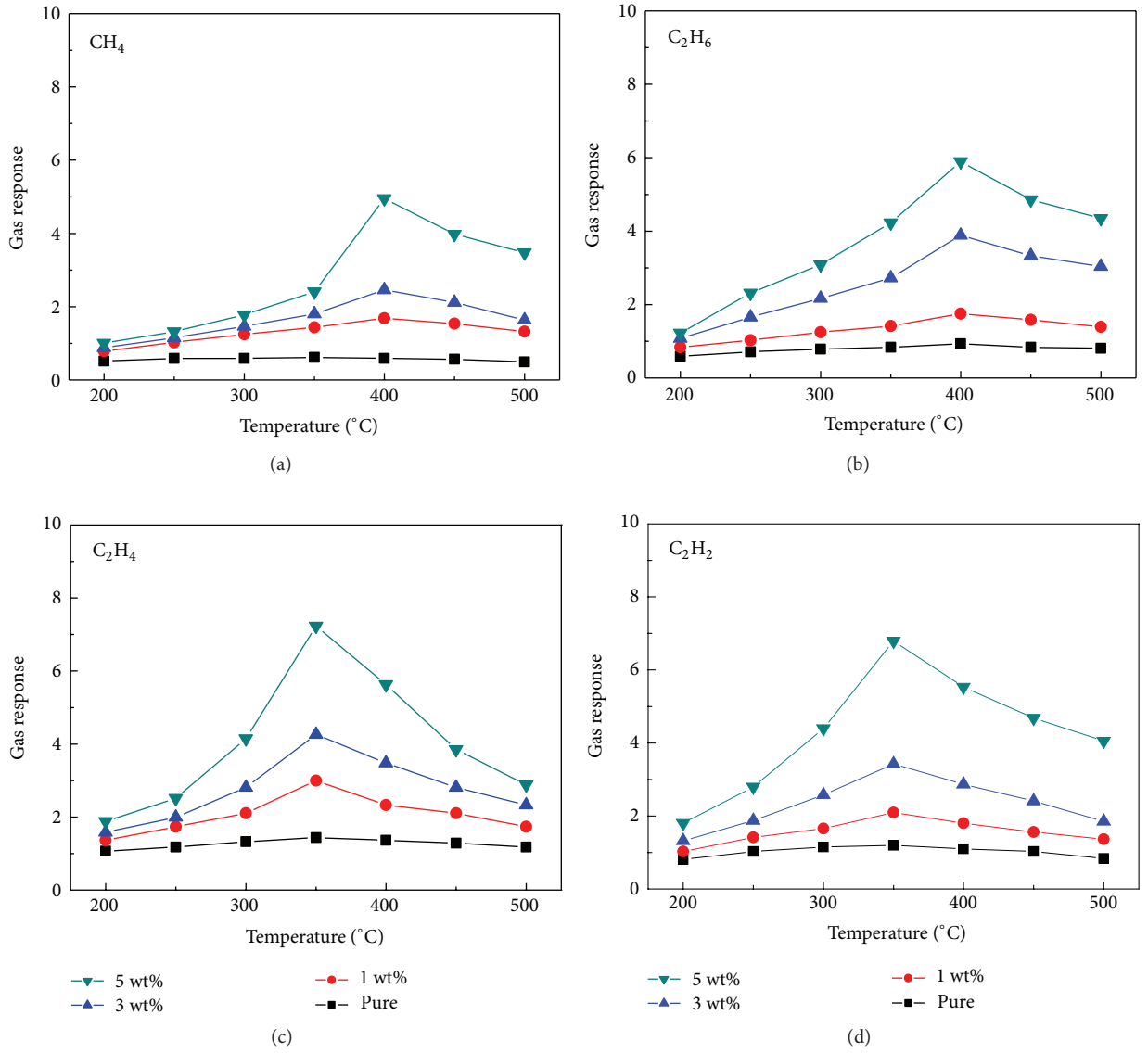

FIGURE 7: Gas responses of the sensors to 100 μL/L of CH_4, C_2H_6, C_2H_4, and C_2H_2 at different operating temperatures (room temperature at 25°C and relative humidity as 60%).

Rutile SnO_2 crystal has four major low-index surfaces (110), (101), (100), and (001) [37, 38]. The (110) surface is the most thermodynamically stable surface and has been widely used to investigate the surface properties of SnO_2. Thus, the density of states (DOS) of SnO_2 (110) surface before and after Pd^{2+}-doping were calculated by replacing partial Sn atoms on the (110) surface (Sn : Pd = 4 : 1). As shown in Figure 6 after Pd^{2+}-doping the DOS of SnO_2 (110) surface shifted downward somewhat, the band gap narrowed and new doping levels appeared near the Fermi level. Pd^{2+}-doping promotes electron transfer between conduction band and valence band and improves the electric conductance properties of the sensor.

The gas responses of these sensors against CH_4, C_2H_6, C_2H_4, and C_2H_2 were measured at different operating temperatures to find out their optimum operating temperatures. The gas responses of the sensors to 100 μL/L of CH_4, C_2H_6, C_2H_4, and C_2H_2 at different operating temperatures were indicated in Figure 7, respectively. For each gas, the gas response values of the sensor increase at different degrees firstly and reach its maximum value at the optimum operating temperature and then decrease rapidly with the operating temperature rising. This tendency is commonly observed in pure and Pd^{2+}-doped SnO_2 sensors. As shown in Figure 7, the optimum operating temperature of the prepared sensor to 100 μL/L of CH_4, C_2H_6, C_2H_4 and C_2H_2 are about 400, 400, 350 and 350°C, respectively, which is attributed to the sensor showing the maximum gas response at the corresponding operating temperature. It is also noted that for each hydrocarbon gas the sensor doped with 5 wt% Pd^{2+} exhibits the highest sensitivity among the four prepared sensors. Correspondingly, when worked at optimum operating

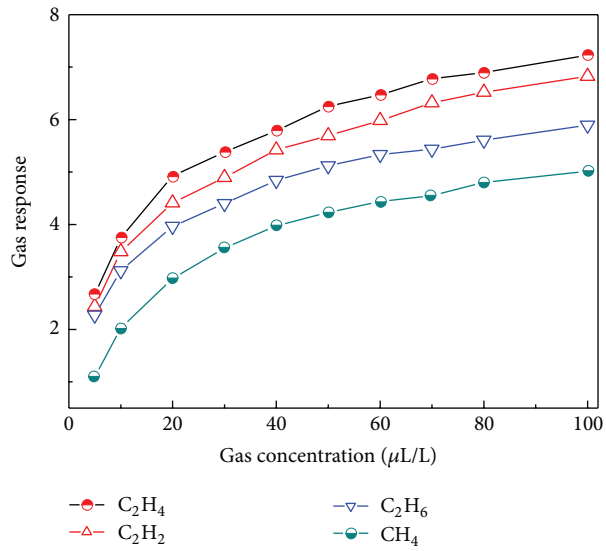

Figure 8: Gas response of the 5 wt% Pd^{2+}-doped sensor to different concentrations of CH_4, C_2H_6, C_2H_4, and C_2H_2 (room temperature at 25°C and relative humidity as 60%).

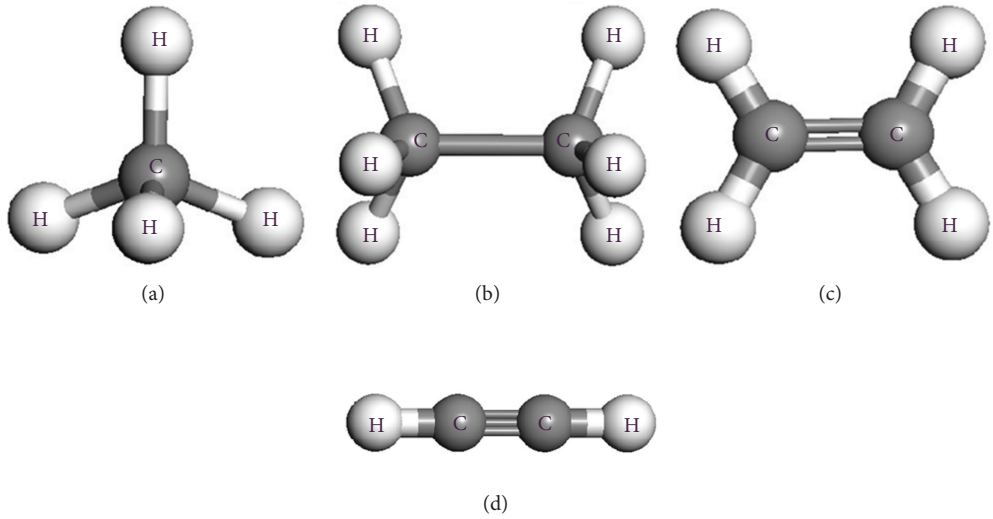

Figure 9: The gas molecule models of CH_4, C_2H_6, C_2H_4, and C_2H_2.

temperatures, the gas responses of the 5 wt% Pd^{2+}-doped sensor against 100 μL/L of CH_4, C_2H_6, C_2H_4, and C_2H_2 are about 4.95, 5.89, 6.78, and 7.22, respectively, which are obviously larger than those of pure 1 and 3 wt% Pd^{2+}-doped sensors.

The gas response of the 5 wt% Pd^{2+}-doped SnO_2 sensor to different gas concentrations of CH_4, C_2H_6, C_2H_4, and C_2H_2 is shown in Figure 8, where the sensor worked at its own optimum operating temperatures as mentioned above. One can clearly see in Figure 8 that with the gas concentration increasing, the gas response of the sensor has an increasing trend in different degrees. Among the four characteristic hydrocarbons, the sensor exhibits maximum response to C_2H_4, followed by C_2H_2, C_2H_6, and CH_4 with a descending order. The relationship between gas response and concentration is quasilinear, which indicates that our prepared sensor can be used to online monitor and detect characteristic hydrocarbon gases dissolved in transformer oil.

Based on the molecular frontier orbital theory, a large number of gas molecular properties are decided by the orbits, particularly HOMO orbits and LOMO orbits [36], which determine the ability of atoms to gain or loss electrons and perform electronic transfer. It is considered that HOMO orbits occupied with the highest energetic electrons are

easy to lose electrons, whereas LUMO orbits occupied with the lowest unoccupied electrons are demonstrated to easily capture electrons during the gas sensing process.

Tin oxide is a typical n-type semiconductor material, and characteristic fault hydrocarbons like CH_4, C_2H_6, C_2H_4, and C_2H_2 are reducing gases. During the gas sensing process, reducing gas molecules manifest to lose electrons, and SnO_2-based gas sensor would capture the same number of electrons lost by adsorbed gas molecules. The electrons received by sensing materials increase the number of carriers and decrease the height of the barrier in the depletion region. In order to further understand the difference of the 5 wt% Pd^{2+}-doped SnO_2 sensor exhibiting various gas responses to hydrocarbon gases, orbital energies of CH_4, C_2H_6, C_2H_4, and C_2H_2 were calculated through the quantum mechanics program. The models of built hydrocarbon gases are shown in Figure 9. After geometry optimization, orbital energy calculations were performed using the $DMol^3$ module.

As shown in Figure 10, the HOMO energy values of CH_4, C_2H_4, C_2H_2, and C_2H_6 are −0.3441, −0.2401, −0.2542, and −0.2995 eV, respectively, and the LUMO energy values for CH_4, C_2H_4, C_2H_2, and C_2H_6 are 0.0834, −0.0272, 0.0121, and 0.0702 eV. Based on the molecular frontier orbital theory, gas molecules easily lose electrons with a higher HOMO. Thus, the ability of losing electron weakens in the following order of C_2H_4, C_2H_2, C_2H_6, and CH_4. The possibility of electron transfer between adsorbed gas molecules and adsorption surface diminishes with the sequence of C_2H_4, C_2H_2, C_2H_6 and CH_4. Because C_2H_4 has the highest HOMO among the four hydrocarbon gases, a relatively higher gas response of the prepared sensor to C_2H_4 is observed. On the contrary, a relatively lower gas response was measured to CH_4. Theoretical calculation results highly agree with our experimental data as mentioned in Figure 8. This finding provides a qualitative understanding for the 5 wt% Pd^{2+}-doped SnO_2 sensor, which indicates different gas responses to CH_4, C_2H_6, C_2H_4, and C_2H_2 with the same gas concentration.

Figure 11 presents the voltage responses of the 5 wt% Pd^{2+}-doped SnO_2 gas sensor to 50 μL/L of CH_4, C_2H_6, C_2H_4, and C_2H_2, where the sensor worked at the optimum operating temperature. It is an intrinsic characteristic of the prepared SnO_2-based sensor that voltage response sharply increased when gas in and dramatically decreased when gas out. As seen in Figure 11, the prepared sensor shows rapid response and recovery to CH_4, C_2H_6, C_2H_4, and C_2H_2, and for each gas, the recovery time is somewhat longer than the response time. Such a rapid response and recovery property could be attributed to the doping effect of the doped metallic ions, which provide some new activity points and catalyze the gas sensing process [29, 33, 34].

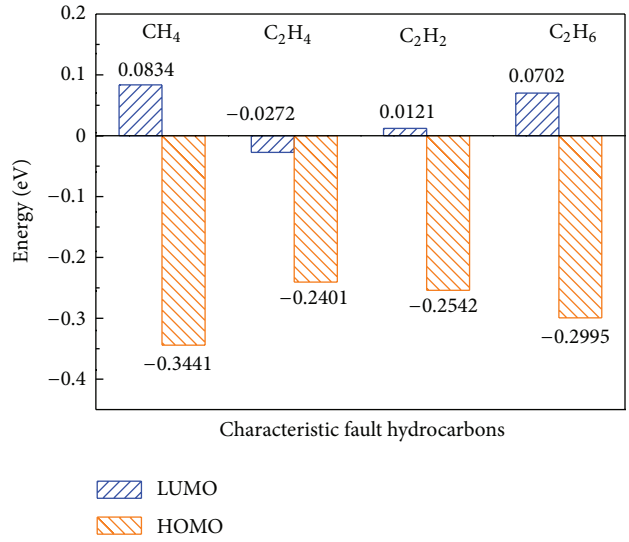

Figure 10: The HOMO and LUMO values of CH_4, C_2H_4, C_2H_2, and C_2H_6.

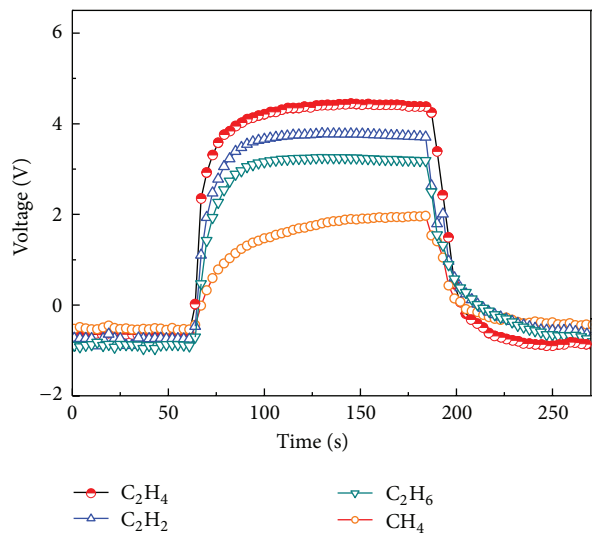

Figure 11: Response and recovery property of the 5 wt% Pd^{2+}-doped sensor to 50 μL/L of CH_4, C_2H_6, C_2H_4, and C_2H_2 (room temperature at 25°C and relative humidity as 60%).

4. Conclusions

Pure and Pd-doped nano-SnO_2 particles were successfully prepared and characterized by XRD, FESEM, and EDS, respectively. The sensor doped with 5 wt% Pd^{2+} ions shows a higher electric conductance and gas sensing properties to characteristic fault hydrocarbons with rapid response and recovery property. The optimum operating temperatures of the 5 wt% Pd-doped sensor are about 400, 400, 350, and 350°C for 100 μL/L of CH_4, C_2H_6, C_2H_4, and C_2H_2 with gas responses of 4.95, 5.89, 6.78, and 7.22, respectively. Based on the molecular frontier orbital theory calculations, the HOMO energy values of CH_4, C_2H_6, C_2H_4, and C_2H_2 are −0.2401, −0.2542, −0.3441, and −0.2995 eV, separately. The ability of lose electrons weakens in the following order: C_2H_4, C_2H_2, C_2H_6, and CH_4. Therefore, the sensor exhibits a larger gas response to C_2H_4 among the four characteristic hydrocarbon gases. These findings provide a further insight to understand different gas sensing properties of the prepared sensors to CH_4, C_2H_6, C_2H_4, and C_2H_2.

Acknowledgments

This work was supported in part by the National Natural Science Foundation of China (no. 51277185), China Postdoctoral Science Foundation (no. 2012M511904), and National Basic Research Program of China (973 Program: 2012CB215205).

References

[1] J. Suonan, K. Liu, and G. Song, "A novel UHV/EHV transmission-line pilot protection based on fault component integrated impedance," *IEEE Transactions on Power Delivery*, vol. 26, no. 1, pp. 127–134, 2011.

[2] J. W. Liu, Y. H. Xiong, and Y. Ji, "The research of the status quo and development of UHV transmission lines construction in China," *Advanced Materials Research*, vol. 516-517, no. 1, pp. 1555–1559, 2012.

[3] I. Villar, U. Viscarret, I. Etxeberria-Otadui, and A. Rufer, "Global loss evaluation methods for nonsinusoidally fed medium-frequency power transformers," *IEEE Transactions on Industrial Electronics*, vol. 56, no. 10, pp. 4132–4140, 2009.

[4] S. M. Markalous, S. Tenbohlen, and K. Feser, "Detection and location of partial discharges in power transformers using acoustic and electromagnetic signals," *IEEE Transactions on Dielectrics and Electrical Insulation*, vol. 15, no. 6, pp. 1576–1583, 2008.

[5] Z. Yang, W. H. Tang, A. Shintemirov, and Q. H. Wu, "Association rule mining-based dissolved gas analysis for fault diagnosis of power transformers," *IEEE Transactions on Systems, Man and Cybernetics Part C*, vol. 39, no. 6, pp. 597–610, 2009.

[6] R. J. Liao, H. B. Zheng, S. Grzybowski, L. Yang, Y. Zhang, and Y. Liao, "An integrated decision-making model for condition assessment of power transformers using fuzzy approach and evidential reasoning," *IEEE Transactions on Power Delivery*, vol. 26, no. 2, pp. 1111–1118, 2011.

[7] A. Akbari, A. Setayeshmehr, H. Borsi, E. Gockenbach, and I. Fofana, "Intelligent agent-based system using dissolved gas analysis to detect incipient faults in power transformers," *IEEE Electrical Insulation Magazine*, vol. 26, no. 6, pp. 27–40, 2010.

[8] H. Xiong, C. X. Sun, R. J. Liao, J. Li, and L. Du, "Study on kernel-based possibilistic clustering and dissolved gas analysis for fault diagnosis of power transformer," *Proceedings of the Chinese Society of Electrical Engineering*, vol. 25, no. 20, pp. 162–166, 2005.

[9] W. G. Chen, Y. X. Yun, C. Pan, and C. X. Sun, "Analysis of infrared absorption properties of dissolved gases in transformer oil," *Proceedings of the Chinese Society of Electrical Engineering*, vol. 28, no. 16, pp. 148–153, 2008.

[10] H. C. Sun, Y. C. Huang, and C. M. Huang, "A review of dissolved gas analysis in power transformers," in *2nd International Conference on Advances in Energy Engineering (ICAEE '12)*, vol. 14, pp. 1220–1225, 2012.

[11] S. Singh and M. Bandyopadhyay, "Dissolved gas analysis technique for incipient fault diagnosis in power transformers: a bibliographic survey," *IEEE Electrical Insulation Magazine*, vol. 26, no. 6, pp. 41–46, 2010.

[12] R. J. Liao, H. B. Zheng, G. Stanislaw, and L. J. Yang, "Particle swarm optimization-least squares support vector regression based forecasting model on dissolved gases in oil-filled power transformers," *Electric Power Systems Research*, vol. 81, no. 12, pp. 2074–2080, 2011.

[13] W. G. Chen, C. Pan, Y. X. Yun, Y. Y. Wang, and C. X. Sun, "Fault diagnosis method of power transformers based on wavelet networks and dissolved gas analysis," *Proceedings of the Chinese Society of Electrical Engineering*, vol. 28, no. 7, pp. 121–126, 2008.

[14] S. Nakata and K. Kashima, "Distinction between alcohols and hydrocarbons with a semiconductor gas sensor depending on the range and frequency of a cyclic temperature," *Analytical Methods*, vol. 4, no. 4, pp. 1126–1131, 2012.

[15] H. T. Giang, H. T. Duy, P. Q. Ngan et al., "Hydrocarbon gas sensing of nano-crystalline perovskite oxides $LnFeO_3$ (Ln = La, Nd and Sm)," *Sensors and Actuators B*, vol. 158, no. 1, pp. 246–251, 2011.

[16] D. Braga and G. Horowitz, "High-Performance organic field-effect transistors," *Advanced Materials*, vol. 21, no. 14-15, pp. 1473–1486, 2009.

[17] F. M. Liu, Y. Q. Zhang, Y. S. Yu, and J. B. Sun, "Enhanced sensing performance of catalytic combustion methane sensor by using Pd nanorod/γ-Al_2O_3," *Sensors and Actuators B*, vol. 160, no. 1, pp. 1091–1097, 2011.

[18] L. Xu, T. Li, X. Gao et al., "Behaviour of a catalytic combustion methane gas sensor working on pulse mode," in *Proceedings of the 9th IEEE Sensors Conference (SENSORS '10)*, pp. 391–394, November 2010.

[19] C. Pijolat, G. Tournier, and J. P. Viricelle, "Detection of CO in H_2-rich gases with a samarium doped ceria (SDC) sensor for fuel cell applications," *Sensors and Actuators B*, vol. 141, no. 1, pp. 7–12, 2009.

[20] Y. Yun, W. Chen, Y. Wang, and C. Pan, "Photoacoustic detection of dissolved gases in transformer oil," *European Transactions on Electrical Power*, vol. 18, no. 6, pp. 562–576, 2008.

[21] W. G. Chen, B. J. Liu, and H. X. Huang, "Photoacoustic sensor signal transmission line model for gas detection in transformer oil," *Sensor Letters*, vol. 9, no. 4, pp. 1511–1514, 2011.

[22] W. Zeng, T. M. Liu, and D. J. Liu, "Hydrogen sensing and mechanism of M-doped SnO_2 (M= Cr^{3+}, Cu^{2+} and Pd^{2+}) nanocomposite," *Sensors and Actuators B*, vol. 160, no. 1, pp. 455–462, 2011.

[23] J. Zhang, S. Wang, M. Xu et al., "Hierarchically porous ZnO architectures for gas sensor application," *Crystal Growth and Design*, vol. 9, no. 8, pp. 3532–3537, 2009.

[24] J. Gong, Y. Li, Z. Hu, Z. Zhou, and Y. Deng, "Ultrasensitive NH_3 gas sensor from polyaniline nanograin enchased TiO_2 fibers," *Journal of Physical Chemistry C*, vol. 114, no. 21, pp. 9970–9974, 2010.

[25] T. Waitz, T. Wagner, T. Sauerwald, C. D. Kohl, and M. Tiemann, "Ordered mesoporous In_2O_3: synthesis by structure replication and application as a methane gas sensor," *Advanced Functional Materials*, vol. 19, no. 4, pp. 653–661, 2009.

[26] Y. Wang, Q. Mu, G. Wang, and Z. Zhou, "Sensing characterization to NH_3 of nanocrystalline Sb-doped SnO_2 synthesized by a nonaqueous sol-gel route," *Sensors and Actuators B*, vol. 145, no. 2, pp. 847–853, 2010.

[27] C. Wang, L. Yin, L. Zhang, D. Xiang, and R. Gao, "Metal oxide gas sensors: sensitivity and influencing factors," *Sensors*, vol. 10, no. 3, pp. 2088–2106, 2010.

[28] Q. Qi, T. Zhang, L. Liu, and X. Zheng, "Synthesis and toluene sensing properties of SnO_2 nanofibers," *Sensors and Actuators B*, vol. 137, no. 2, pp. 471–475, 2009.

[29] T. Zhang, L. Liu, Q. Qi, S. Li, and G. Lu, "Development of microstructure In/Pd-doped SnO_2 sensor for low-level CO detection," *Sensors and Actuators B*, vol. 139, no. 2, pp. 287–291, 2009.

[30] X. Song, Q. Qi, T. Zhang, and C. Wang, "A humidity sensor based on KCl-doped SnO_2 nanofibers," *Sensors and Actuators B*, vol. 138, no. 1, pp. 368–373, 2009.

[31] Y. Shen, T. Yamazaki, Z. Liu, D. Meng, and T. Kikuta, "Hydrogen sensors made of undoped and Pt-doped SnO_2 nanowires," *Journal of Alloys and Compounds*, vol. 488, no. 1, pp. L21–L25, 2009.

[32] Y. C. Lee, H. Huang, O. K. Tan, and M. S. Tse, "Semiconductor gas sensor based on Pd-doped SnO_2 nanorod thin films," *Sensors and Actuators B*, vol. 132, no. 1, pp. 239–242, 2008.

[33] S. Wang, Y. Zhao, J. Huang et al., "Low-temperature CO gas sensors based on Au/SnO_2 thick film," *Applied Surface Science*, vol. 253, no. 6, pp. 3057–3061, 2007.

[34] Y. B. Xue and Z. A. Tang, "Density functional study of the interaction of CO with undoped and Pd doped SnO_2(110) surface," *Sensors and Actuators B*, vol. 138, no. 1, pp. 108–112, 2009.

[35] F. Trani, M. Causà, D. Ninno, G. Cantele, and V. Barone, "Density functional study of oxygen vacancies at the SnO_2 surface and subsurface sites," *Physical Review B*, vol. 77, no. 24, Article ID 245410, 8 pages, 2008.

[36] Z. Wen and L. Tian-mo, "Gas-sensing properties of SnO_2-TiO_2-based sensor for volatile organic compound gas and its sensing mechanism," *Physica B*, vol. 405, no. 5, pp. 1345–1348, 2010.

[37] Z. Wen, L. Tian-Mo, and L. Xiao-Fei, "Hydrogen sensing properties of low-index surfaces of SnO_2 from first-principles," *Physica B*, vol. 405, no. 16, pp. 3458–3462, 2010.

[38] J. Oviedo and M. J. Gillan, "Energetics and structure of stoichiometric SnO_2 surfaces studied by first-principles calculations," *Surface Science*, vol. 463, no. 2, pp. 93–101, 2000.